Analysis of ultrafast X-ray diffraction data in a linear-chain model of the lattice dynamics

6 **AUTHORS**, INCLUDING:

Marc Herzog

Fritz Haber Institute of the Max Planck Soci…

27 PUBLICATIONS 175 CITATIONS

Daniel Schick

Helmholtz-Zentrum Berlin

23 PUBLICATIONS 112 CITATIONS

Peter Gaal

University of Hamburg

44 PUBLICATIONS 658 CITATIONS

Roman Shayduk

Deutsches Elektronen-Synchrotron

40 PUBLICATIONS 258 CITATIONS

Analysis of ultrafast X-ray diffraction data in a linear-chain model of the lattice dynamics

**M. Herzog · D. Schick · P. Gaal · R. Shayduk ·
C. v. Korff Schmising · M. Bargheer**

Abstract We present ultrafast X-ray diffraction (UXRD) experiments which sensitively probe impulsively excited acoustic phonons propagating in a $SrRuO_3/SrTiO_3$ super-lattice and further into the substrate. These findings are discussed together with previous UXRD results (Herzog et al. in Appl. Phys. Lett. 96, 161906, 2010; Woerner et al. in Appl. Phys. A 96, 83, 2009; v. Korff Schmising in Phys. Rev. B 78, 060404(R), 2008 and in Appl. Phys. B 88, 1, 2007) using a normal-mode analysis of a linear-chain model of masses and springs, thus identifying them as linear-response phenomena. We point out the direct correspondence of calculated observables with X-ray signals. In this framework the complex lattice motion turns out to result from an interference of vibrational eigenmodes of the coupled system of nanolayers and substrate. UXRD in principle selectively measures the lattice motion occurring with a specific wavevector, however, each Bragg reflection only measures the amplitude of a delocalized phonon mode in a spatially localized region, determined by the nanocomposition of the sample or the extinction depth of X-rays. This leads to a decay of experimental signals although the excited modes survive.

M. Herzog · D. Schick · P. Gaal · M. Bargheer (✉)
Institute of Physics and Astronomy, University Potsdam,
Karl-Liebknecht-Strasse 24-25, 14476 Potsdam, Germany
e-mail: bargheer@uni-potsdam.de

R. Shayduk · M. Bargheer
Helmholtz-Zentrum Berlin für Materialien und Energie GmbH,
Hahn-Meitner-Platz 1, 14109 Berlin, Germany

C. v. Korff Schmising
Atomic Physics Division, Department of Physics, Lund
University, P.O. Box 118 22100 Lund, Sweden

1 Introduction

Ultrafast X-ray diffraction (UXRD) is capable of monitoring atomic motion in solids on the atomic length and timescale. It has been applied to the study of optical and acoustic phonons and in particular to zone-folded longitudinal acoustic phonons (ZFLAPs) in superlattices (SLs), which can be viewed as acoustic or optical phonons, from the perspective of the bulk or the SL-mini-Brillouin zone, respectively [5, 6]. In theory, the mini-Brillouin zone is defined for an infinite SL. Experimentally, this is approximated by periodically stacking a large number P of epitaxial double layers of two different crystal lattices (e.g. GaAs/AlGaAs) on top of each other. Such a SL with $P = 2000$ and a double layer period d_{SL} was recently investigated after homogeneous excitation with femtosecond laser pulses [7]. The resulting standing strain wave was essentially an optical phonon with wavevector $Q = 0$, as it corresponded to the motion of atoms within the super unit cell (one double layer GaAs/AlGaAs) and to a good approximation the substrate could be neglected. No lineshift of the Bragg reflection was observed, evidencing that the size of the super unit cell remained constant on the timescale of the experiment. When the number P of double layers is smaller, e.g. $P = 11$, as was the case in a previously studied oxide SL of $SrRuO_3/SrTiO_3$ (SRO/STO), the coupling to the substrate leads to a decay of the SL motion [1–4, 8]. The timescale of this decay is set by the SL expansion time, corresponding to the time $T = D/v_{SL} \approx 35$ ps it takes an acoustic phonon to traverse the SL thickness $D = P \cdot d_{SL} \approx 250$ nm at the average sound velocity v_{SL} [9, 10].

A key advantage of UXRD is the direct correspondence of the real-space periods with the wavevector transfer $\mathbf{q} = \mathbf{k} - \mathbf{k}' = \mathbf{G} \pm \mathbf{Q}$ encoded in a generalized Laue condition, where $G = |\mathbf{G}| = 2\pi/c$ is a reciprocal lattice vector corresponding to the real-space lattice spacing c and $\mathbf{Q}$ is the

wavevector of a specific phonon mode. In SLs $G = n \cdot g$ ($n \in \mathbb{N}$) is an integer multiple of the reciprocal SL vector $g = 2\pi/d_{SL}$ [11]. The first achievement of UXRD was to show that coherent acoustic phonons in bulk lattices lead to a temporal modulation of the X-ray diffraction signal at $G \pm Q$ according to the phonon dispersion relation $\omega(Q)$ [12–14]. The SL phonon modes exhibit a time dependence according to their frequency $\omega_{SL} = \omega(Q = 0)$ as an intensity modulation of the SL Bragg peak, as they are optical modes at the mini-Brillouin zone center ($Q = 0$). Exciting a thin Ge film resulted in sidebands to the bulk reflection of a Si substrate at G_{Si} and a continuous shift and broadening of the Ge reflection at G_{Ge} [15]. Experiments on InGaAs/InAlAs SLs also reported shifts of the SL Bragg peaks, and in addition the "unfolding" of the SL phonon with wavevector Q_{SL} into the InP substrate leading to new reflections at $G_{sub} \pm Q_{SL}^*$ [16]. In all these cases, the excitation of a broad acoustic phonon spectrum leads to a continuous shift of peaks or the development of a sideband to an existing peak.

In this paper we present UXRD measurements on a photoexcited SRO/STO SL that shows the disappearance of a Bragg reflection at a particular $G = n \cdot g$ and its reappearance at a different $G' = n \cdot g'$ corresponding to an expanded SL without exhibiting a continuous shifting of the rocking curve. In addition, very clear sidebands to the bulk substrate reflection show up. Continuous shifts as well as sidebands of thin film and substrate Bragg peaks have been previously discussed in the context of acoustic sound propagation [12–18]. Here, we focus on analysing such features, including recently published UXRD data on the same SRO/STO SL, within a simple linear-chain model which describes the longitudinal phonon spectrum of the SL on a substrate. We discuss in detail which modes are optically excited and how this gives rise to both propagating and standing waves in the structure. We analyze how the different features of the lattice dynamics can be directly measured and calibrated by UXRD and calculate rocking curves using dynamical X-ray diffraction theory. It turns out that the disappearance and reappearance or rather splitting of the Bragg peak reflects the short-timescale dynamics of the coherent acoustic phonon spectrum within the SL for strong excitation. The sidebands of the substrate peak measure the appearance of this coherent wavepacket distortion in the substrate, whereas the appearance of the $G_{sub} \pm Q_{SL}^*$ peaks [16] show the spatial period of the SL phonon after it has propagated (unfolded) into the substrate. All these phenomena are quantitatively predicted by the presented model and therefore identified as a linear response of the sample.
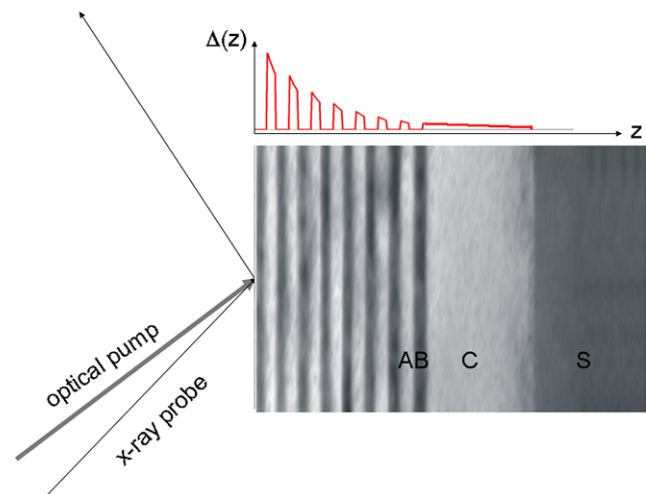
2 Experiments

2.1 Results

Figure 1 shows the TEM cross section of the SRO/STO SL together with a schematic of the experiment. An optical pump pulse is absorbed by the metallic SRO layers of the sample leading to a quasi-instantaneous spatial stress profile $\Delta(z)$ indicated by the red line. A time-delayed X-ray probe pulse measures the excited sample by diffraction of monochromatic X-ray photons impinging on the sample at different Bragg angles.

We used the laser-based femtosecond X-ray diffractometer at University of Potsdam, which is very similar to the one described recently [19], for measuring a particular SL reflection, whereas transients of the STO substrate peak were recorded at the Femto-slicing beamline of the Swiss Light Source (SLS) [20]. The inset of Fig. 2 shows an overview of the sample's diffraction profile around the bulk (0 0 2) reflection of the substrate. The time dependence of the strongest SL peak with the SL-Miller index (0 0 116) has been characterized previously according to its so-called shift within 30 ps and its intensity modulation which shows a period of 3.2 ps due to the SL phonon [1–4]. This modulation decays with a similar time constant of approx. 30 ps.

A new and more detailed set of experimental results on this (0 0 116) reflection is presented in Fig. 2. We measured the time-dependent diffracted X-ray intensity $I(q, t)$ for different wavevector transfers $q = \sin(\theta)4\pi/\lambda$. The Bragg reflectivity is defined by $R(q, t) = I(q, t)/I_0(q)$, where $I_0(q)$ is the X-ray intensity incident on the sample. Figure 2(c) shows the difference spectra $R(q, t) - R_0(q)$, i.e.,
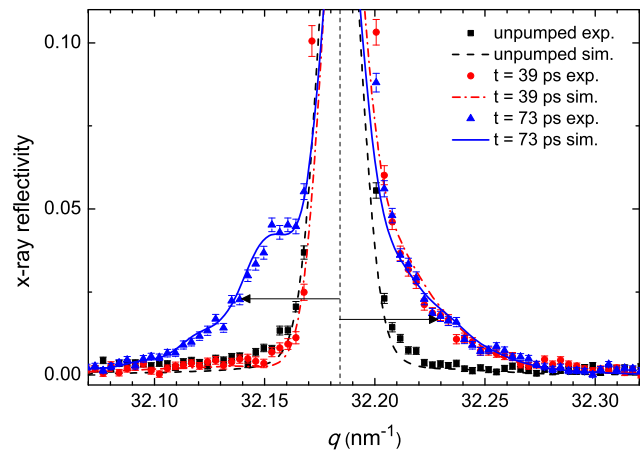

Fig. 1 Schematic of the experiment. An optical laser pulse excites a SL sample with the stacking sequence $(B_n/A_m)_P C S$ (shown here as a TEM image), generating a stress profile $\Delta(z, t = 0)$ (*upper panel*). In the particular sample shown $A = \text{SRO} = \text{SrRuO}_3$, $B = \text{STO} = \text{SrTiO}_3$, contact layer $C = A$ and substrate $S = B$
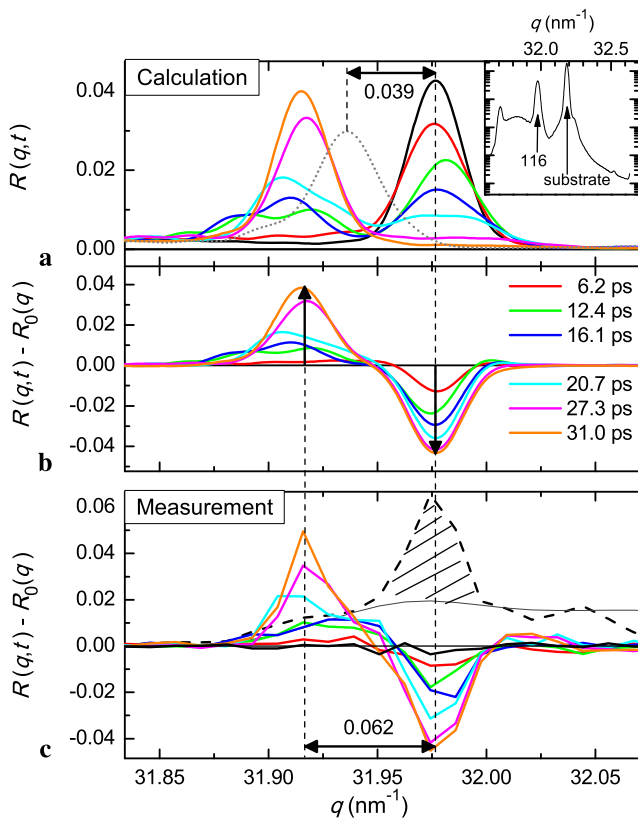
Fig. 2 (**a**) Calculated rocking curves in the vicinity of the (0 0 116) SL reflection as a function of pump-probe time delay. The short dashed line shows the peak after the strain waves have left the SL ($t \gtrsim 70$ ps). *Inset*: Extended rocking curve including the (0 0 2) STO substrate peak [1]. (**b**) Derived difference rocking curves with same color code for $t > 0$. (**c**) Measured unpumped rocking curve (*dashed line*) including background contribution (*thin black line*). The *thick black line* shows the difference curve for $t = 0$. Other lines show the measured difference rocking curves with the same color code as in panel (**a**)

Fig. 3 X-ray diffraction curves in the vicinity of the (0 0 2) STO substrate reflection. *Symbols* report the measured data, *lines* correspond to simulations (see text). At 39 ps (73 ps) after the laser-pulse excitation a compression (expansion) wave has entered the substrate, giving rise to the shoulder on the high-angle (low-angle) side. The asymmetry originates from complex interferences of the X-rays from the distorted and undistorted parts of the substrate

the changes of the Bragg-reflectivity curve of the sample for a specific time delay t with respect to the spectra averaged over time delays before the excitation pulse $R_0(q) = R(q, t \leq 0)$ (dashed line). This procedure removes a background contribution to the signal (thin black line) which originates from the focusing of X-rays by a multilayer mirror and leads to signals on the X-ray CCD detector at all angles. For comparison, panel (b) shows the good agreement to the corresponding difference spectra from the simulation (see theory section) and panel (a) shows the calculated spectra directly, clearly representing the disappearance of the right peak and its reappearance to the left. Note that the appearing peak has strongly shifted components around 31.9 nm^{-1} for early times ($0 < t < 20$ ps) and it slightly moves back toward larger angles at later times ($t > 20$ ps). The details such as height, position and shape of the peaks in the experimental and calculated difference spectra show excellent agreement. The spectrum for $t = 0$ (thick black line in Fig. 2(c)) demonstrates that the difference spectra ac-

tually lead to a correct subtraction of the unwanted background as the experimentally measured difference signal is approximately zero.

Without detailed simulation, the splitting of the SL-Bragg peak for intermediate times can be attributed to two regions of the SL, one having the static spatial SL-period d_{SL} (right peak) and one exhibiting an expanded lattice. The maximum strain of the entire SL occurs at a time delay of approx. 35 ps and is calculated by

$$\epsilon_{\max} = \frac{D_{\max} - D(0)}{D(0)} = \frac{q_{\max}^{-1} - q(0)^{-1}}{q(0)^{-1}} \quad (1)$$

From Fig. 2 we read $\epsilon_{\max} \approx 0.062/31.975 = 1.9 \cdot 10^{-3}$. This experiment was performed at the femtosecond X-ray diffractometer in Potsdam with laser pulses (≈ 100 fs, 800 nm) at a fluence of approx. 10 mJ/cm^2.

In addition, we monitored the shoulders of the STO substrate reflection with a higher angular resolution by performing diffraction experiments with the highly collimated X-rays at the FEMTO-slicing beamline at the SLS. The resulting rocking curves recorded under somewhat increased fluence and at 400 nm pump wavelength are presented in Fig. 3. Cross-checks with 800 nm pump pulses show similar results. From the angular separation of the shoulder from the substrate peak we can estimate the amplitude of the strain wave in the substrate to be $\epsilon_{STO} = \Delta c/c = 0.04/32.2 \approx 1.24 \cdot 10^{-3}$, which is slightly smaller than the expansion of the SL observed above.

2.2 Discussion of results

In the following we discuss how the total optical excitation energy is deposited in the lattice. Using the absorption depth $\zeta_{SRO} = 52$ nm and the absorbed pump fluence $F \approx 10$ mJ/cm^2, the energy density absorbed by the conduction band electrons of SRO in each layer exponentially decays from $\rho_E^{SRO} \approx 1.8 \cdot 10^9$ J/m^3 in the first to $\rho_E^{SRO} \approx 4.3 \cdot 10^8$ J/m^3 in the tenth layer [1]. This energy is then coupled to phonons of SRO on a 100 fs timescale which essentially leads to the expansion of the SRO layers [1–4]. We assume that the expansion of the SL is induced exclusively by an expansion of SRO layers with a linear thermal expansion coefficient $\alpha_{SRO} = 1 \cdot 10^{-5}$ K^{-1} and a volumetric heat capacity $C_{SRO}^{heat} = 3 \cdot 10^6$ J/(K m^3) of SRO [9]. The average deposited energy density $\rho_{av}^{SRO} \approx 1.04 \cdot 10^9$ J/m^3 in the SRO layers then corresponds to a temperature rise of $\Delta T = \rho_{av}^{SRO}/C_{SRO}^{heat} \approx 347$ K. The relative expansion of the entire SL due to the exclusive expansion of SRO is $\epsilon(\Delta T) = d_{SRO}\alpha\,\Delta T/d_{SL} \approx 1.2 \cdot 10^{-3}$ which is similar to ϵ_{max}.

In a next step, we calculate the energy density transferred to coherent acoustic strain in the SL and later on in the substrate from the measured UXRD data. First, we estimate the amount of energy in the coherent acoustic modes that lead to the observed maximum shift of the SL reflection (Fig. 2). The elastic modulus $E = v_{SL}^2 \cdot \rho$ is calculated from the averaged longitudinal sound velocity v_{SL} and the mass density ρ of STO and SRO. From the observed maximum strain ϵ_{max} in the SL with a thickness of $D = 250$ nm we infer the deformation energy density of the SL, i.e. the integrated energy in the longitudinal acoustic modes, to be $\rho_{LA}^{SL} = 1/2 E \epsilon_{max}^2 = 5.3 \cdot 10^5$ J/m^3, corresponding to a fraction of approx. $5.2 \cdot 10^{-4}$ of the optically deposited energy density. We will see in the discussion of the theory section that this overestimates the coherent sound energy. In fact, not the maximally shifted curve in Fig. 2(a) but rather the gray dotted curve shows the peak shift corresponding to the heat expansion $\epsilon_{heat} = 1.2 \cdot 10^{-3}$ of the sample which—as we will show—also corresponds to the amplitude of the coherent strain wave.

Second, we alternatively consider the observed shoulders of the substrate peak in Fig. 3. As no heat is deposited in the substrate, the lattice deformation indicated by these shoulders must originate from the coherent sound waves propagating into the substrate. In the theory section we will show that in fact both the splitting of the SL peak and the substrate peak shoulders probe the same superposition of eigenmodes, however, the SL peak probes these delocalized phonons locally within the 250 nm thick SL, whereas the substrate shoulders probe the same modes locally in the first few microns of the substrate. During the propagation into the substrate the ratio of the sound velocities $s = v_{STO}/v_{SL} \approx 1.3$

leads to a traveling wave with total length of $l_W = 2sD = 650$ nm (compressive + tensile part). The average compressive and tensile strain ϵ_{STO} inferred from the substrate peak shoulders on the high-q and low-q side, respectively, yields an energy density $\rho_{LA}^{STO} = 3.5 \cdot 10^5$ J/m^3. Comparing this to ρ_{LA}^{SL} one finds that the energy density of the coherent sound is smaller in the substrate, however, the acoustic energy fluence $F_{LA} = \rho_{LA}^{STO} \cdot l_W \approx \rho_{LA}^{SL} \cdot D$, i.e., the coherent acoustic energy per excited sample area, is conserved (cf. Fig. 7).

This implies that at the used pump fluence, only a fraction of $F_{LA}/F = 5 \cdot 10^{-4}$ of the deposited energy is converted into coherent acoustic waves, whereas the rest remains as incoherent phonons, i.e. lattice heat. Note that the energy density ρ_{LA} of the coherent wave is proportional to the square of the strain ϵ^2, whereas the deposited heat energy ρ_{av}^{SRO} is proportional to ϵ according to linear heat expansion. For lower fluences an even smaller fraction of light energy is converted to the coherent sound wave.

3 Theory

In order to analyze the experimental results quantitatively, to visualize the dynamics and to verify that even under such strong excitation the response of the sample is still linear, we set up a linear-chain model of masses and springs. A similar linear-chain model was presented in Ref. [21] for the discussion of ultrafast electron diffraction data on a thin metal film. In the following we describe the extension to superlattices. More importantly, we present a normal-mode analysis of this linear-chain model and discuss how this is relevant to the interpretation of diffraction data.

3.1 Linear-chain model

We consider a multilayer with the stacking sequence $(B_n/A_m)_P CS$ composed of m unit cells of an opaque material A and n unit cells of a transparent material B epitaxially grown as a SL with P periods on a virtually infinitely thick and transparent substrate S with a thin contact (electrode) layer C (cf. Fig. 1). The SL is excited with an ultrashort optical light pulse. This heats up the opaque layers A and induces expansive thermal stress $\Delta(z)$ on a timescale τ_Δ short compared to all atomic motions that are of interest in this paper ($\tau_\Delta \ll 1/\omega_{SL}$). The excitation stress $\Delta(z_A) \sim e^{z_A/\zeta_A}$ varies as a function of penetration depth z_A through opaque layers A and is basically determined by the bulk optical absorption length ζ_A. As a first approximation, we assume that on the timescale of interest, the thermal stress remains constant after the excitation, i.e. $\Delta(z,t) = \Delta(z)H(t)$, where $H(t)$ is a Heaviside step function in time t. In other words, we disregard slow cooling by heat conduction. This assumption is justified independent of the photon energy [3]. We

disregard the distinction of electron and phonon contributions to the stress [21] as this should only marginally affect the timing in our experiments.

For the simulation of acoustic waves in the structure we construct a one-dimensional model of N masses and springs along the z-direction (c-axis), where each unit cell is represented by a mass m_A, m_B, m_C and m_S, respectively, which are connected by springs having a force constant $k_i = m_i v_i^2 / c_i^2$. Here v_i is the longitudinal sound velocity, m_i is the mass and c_i is the out-of-plane lattice constant of the ith unit cell ($i = 1, 2, \ldots, N$).[1] This model allows for the simulation of all longitudinal acoustic modes propagating perpendicular to the surface of the sample. It neglects longitudinal optical modes of the bulk crystals A, B, C and S and all transverse motions. Alternatively, one could follow a continuum-model approach [6], however, here we want to focus on a normal-mode analysis.

To calculate the displacements $x_i(t) = z_i(t) - z_i^0$ from the equilibrium positions z_i^0 in a linear chain of N masses m_i that are connected by springs with force constants k_i and are subject to an additional force $F_i(t)$ (optically induced stress), we have to solve a system of N linear inhomogeneous differential equations

$$m_i \ddot{x}_i = -k_i(x_i - x_{i-1}) - k_{i+1}(x_i - x_{i+1}) + F_i(t) \qquad (2)$$

where $i = 1, \ldots, N$.

Unlike Ref. [21] we do not solve this set of equations by numerical integration (such as Runge–Kutta methods) but rather find the general solution

$$\mathbf{X}(t) = \sum_{j=1}^{N} \Xi_j \cdot A_j e^{i\omega_j t}. \qquad (3)$$

by diagonalization of the force matrix (see Appendix) in terms of eigenvectors Ξ_j to the eigenvalues (eigenfrequencies) ω_j of the system, which in fact represent the acoustic phonon modes of this nanostructure. $\mathbf{X}(t)$ is a vector containing the time-dependent coordinates $x_i(t)$ of all masses. The appropriate boundary condition is depicted in Fig. 4 which shows that at $t = 0$ the springs are quasi-instantaneously compressed (laser induced stress $\Delta(z)$ in SRO) and subsequently evolve toward the configuration for $t \to \infty$ where all springs attain their original length.

We use the physical insight that the additional time-independent forces proportional to $\Delta(z)$ trigger a "displacive excitation of coherent phonons" (DECP) by displacing the equilibrium position of the masses. Since the essential effect of heating material A is its expansion while keeping the compressibility constant, we can visualize this

---

[1]This corresponds to an elastic modulus $E = \rho v^2$ in a continuum-model approach.
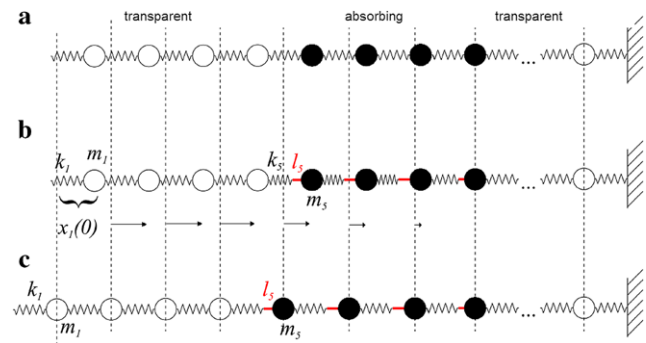
Fig. 4 Schematic of the linear-chain model. (**a**) For $t < 0$ all masses are at rest. (**b**) At $t = 0$ an excitation stress Δ is induced, which is subsequently constant. In the linear-chain schematic it is represented by incompressible sticks, which lead to an instantaneous compression of the springs in the opaque material A. The force constant of the springs remains unchanged. For $t > 0$ masses move according to the new forces. (**c**) Rest positions of masses x^∞ for $t \to \infty$

process by instantaneously inserting incompressible spacer sticks between the springs and the atoms, which have a length proportional to $\Delta(z)$ (see Fig. 4(b)). After very long times ($t \to \infty$), the linear chain would relax into configuration (Fig. 4(c)) where all springs are at their equilibrium length, which they had before excitation (Fig. 4(a)). After solving the equations for all coordinates $x_i(t)$, one can now analytically calculate the relative displacement of the masses $\Delta x_i = x_i - x_{i-1}$ and the corresponding strain $\epsilon_i = [\Delta x_i(t) - \Delta x_i(0)] / \Delta x_i(0)$ for any time t and any given initial stress profile $\Delta(z)$.

This model contains no anharmonic interaction potential and we expect a linear response of the lattice dynamics proportional to the excitation stress $\Delta(z)$. The amplitude of $\Delta(z)$ is the only fitting parameter in this simulation. The lattice parameters, elastic constants, heat capacity etc. are taken from the literature, as well as the absorption length ζ_A. The calibration of the stress amplitude is simply achieved by matching the experimentally observed change of SL-Bragg angle to the average lattice expansion. Figure 5 shows the result of such a calculation for an SRO/STO SL including the ≈ 42 nm SRO contact layer [1] with an absorption length of the optical excitation light of $\zeta_{SRO} = 52$ nm [22]. Both standing strain wave contributions with the spatial period of the SL and propagating strain waves can be seen in this contour plot. The slopes of the diagonal stripes directly visualize the local average sound velocity $v_{SL} = \Delta z / \Delta t$, which is slightly different in the SL, contact layer and substrate.
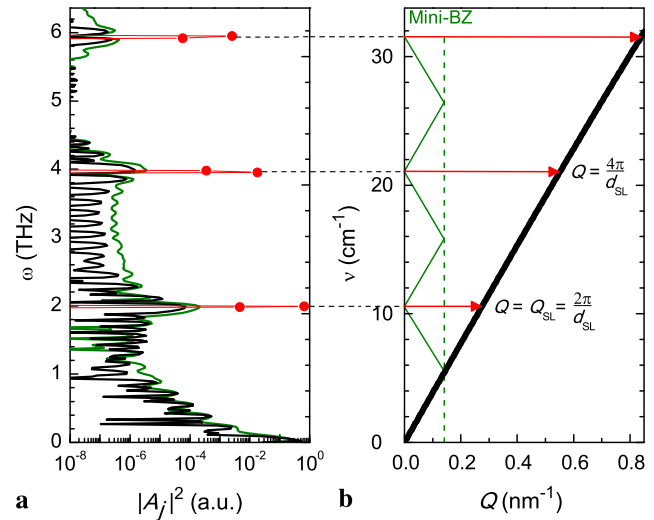
In order to discuss the significance of eigenmodes in SLs we compare the situation of a few-period SL with $P = 11$ to an infinite SL by imposing periodic boundary conditions. Such an infinite SL was well approximated in the experiments on a GaAs/AlGaAs SL with $P = 2000$ [7, 23]. For better comparison, the present calculation is performed for the SRO/STO SL discussed above using periodic boundary
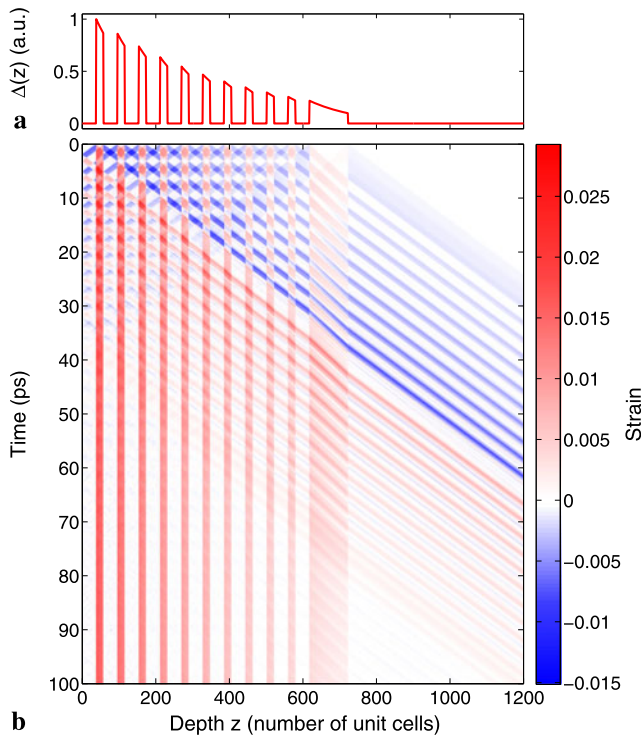
Fig. 5 (**a**) Stress profile $\Delta(z, t = 0)$. (**b**) Contour plot showing the calculated strain in the sample as a function of space and time for the SRO/STO SL investigated experimentally [1–4]

Fig. 6 (**a**) Phonon population spectrum of strain evolution decomposed into amplitudes $|A_j|^2$ of eigenmodes to eigenfrequency ω_j for the infinite SRO/STO SL (periodic boundary condition) with homogeneous excitation ($\zeta_{SRO} \to \infty$, *red dots*) and for the finite SL ($P = 11$) with homogeneous excitation (*thin green line*) and the experimental optical penetration depth of $\zeta_{SRO} = 52$ nm (*thick black line*). Note that for the infinite SL single mode is excited. (**b**) Dispersion relation of a SL from linear-chain model (*thick black line*) back-folded into the mini-Brillouin zone (*thin blue line*)

conditions. Plotting the eigenfrequencies ω_j as a function of the normal-mode wavevector Q_j visualizes the phonon dispersion relation $\omega(Q)$ (cf. Fig. 6(b)). For a SL it is useful to recall that the dispersion relation can be represented in a smaller mini-Brillouin zone, where the zone boundary is given by π/d_{SL} instead of π/c if d_{SL} is the thickness of one SRO/STO double layer. Figure 6(a) compares the squared modulus $|A_j|^2$ of the complex amplitudes for the eigenmodes with frequency ω_j (cf. (3)) in an infinite SL with homogeneous excitation ($\zeta \to \infty$, red dots), in the $P = 11$ SL with homogeneous excitation (thin green line) and in the $P = 11$ SL with the experimental absorption length of $\zeta_{SRO} = 52$ nm (black) [22]. As the spatial symmetry of the excitation pattern $\Delta(z)$ intrinsically mimics the symmetry of the SL, only eigenmodes with a wavevector equal to integer multiples of the reciprocal SL wavevector $Q_{SL} = g = 2\pi/d_{SL}$ are selected. For an infinite SL such modes are optical phonons at the zone center of the mini-Brillouin zone scheme (zone-folded dispersion relation plotted in green in Fig. 6(b)). In this case only few modes are excited. One of them has almost unit probability and we refer to it as the symmetric SL mode with period $T_{SL} = 2\pi/\omega_{SL}$, as it corresponds to an expansion of the SRO layers symmetric with respect to the center of the SRO layer [5]. The related asymmetric mode and all higher harmonics have at least two orders of magnitude less weight. Note that the splitting of the symmetric and asymmetric mode is very

small ($\Delta\omega/\omega = 4.5 \cdot 10^{-5}$), indicating an excellent acoustic impedance matching, which is evident also from Fig. 5 where almost the entire soundwave is transmitted to the substrate with essentially zero reflection amplitude.

If we simulate a finite SL, i.e., we do not consider the periodic boundary condition, and add a substrate beneath the SL, the symmetry is broken by both the surface of the SL and the interface to the substrate. Under these conditions, several modes are excited with considerable amplitude (cf. green curve in Fig. 6(a)). The mode density in the simulation depends on the number of substrate unit cells taken into account, however, clearly the modes in the vicinity of the SL mode and its harmonics still have enhanced weight. Here we chose the substrate approximately three times thicker than the SL, in order to prevent reflections from the backside within the simulated timescale in Fig. 5(b). It is the breaking of the symmetry by the surface and the substrate that induces the high occupation of low-frequency modes near $\omega = 0$ indicating a propagating sound wave. If the excitation is changed to the exponentially decaying absorption of energy in the SL, only slight modifications of the phonon population spectrum $|A_j(\omega)|^2$ is observed.

There are several advantages of the normal-mode analysis as compared to a numerical propagation of the differential equation [21]: (i) It allows rapid calculation of strain pattern for any time t. (ii) Individual modes can be switched off to disentangle complex dynamics. (iii) The wavevector Q of each mode predicts where the corresponding time dependence will show up in the UXRD signal. (iv) Wavepacket

dynamics including the coupling of SL and substrate is interpreted as interference of waves.

3.2 Comparison to experimental data

We first discuss the coarse findings depicted in Fig. 5. For the SL coupled to the substrate, several eigenmodes in the vicinity of ω_{SL} with approximately equal spatial periodicity are excited, however, they extend into the substrate with similar amplitude as well. According to the mini-BZ scheme, at early times these modes give rise to a standing wave composed of waves with $-Q_{SL}$ propagating toward the surface and Q_{SL} propagating toward the substrate. This standing wave pattern which is localized in the SL disappears when all waves have propagated into the substrate and hence no time dependence with frequency ω_{SL} remains in the SL. The waves leave the multilayer as propagating sound waves having the central frequency of the SL mode and the wavevector $Q^*_{SL} = 2\pi/d^*_{SL}$, which is determined by the ratio of the substrate sound velocity v_{STO} and the average sound velocity in the SL, i.e., $d^*_{SL} = v_{STO}T_{SL} = d_{SL} \cdot v_{STO}/v_{SL}$ [16]. The higher harmonics of the SL mode with frequency $\omega_{SL} = 2\pi/T_{SL}$ also show considerable—albeit much smaller—amplitudes and support the spatiotemporal sharpness of the sound features observed in Fig. 5. In previous experiments, these folded acoustic phonons at ω_{SL} were observed as intensity modulations of the SL Bragg reflections [1–4]. In a SL these phonons are back-folded to $Q = 0$ (green dispersion relation in Fig. 6), and hence they show up in the UXRD measurements at the Bragg angle of stationary SL reflections. When the wavepacket has traveled into the substrate, these modes yield sidebands to the substrate at $G_{STO} \pm n Q^*_{SL}$, where n is an integer [16]. The origin of these modes can be seen by the small wavelets that are generated at each interface of the SL.

The surface and the contact layer (interface to the substrate) are the spatial origin of the low-frequency modes [cf. Fig. 5(b)]. The reflection of the compressive wavepackets at the surface results in an expansion wave traveling straight through the SL into the substrate with marginal reflection an the interface. The contact layer launches a compression wave into the substrate and another one toward the surface, where it is converted into an expansion wave. Inspection of the average strain per double layer in Fig. 5(b) at around 15–20 ps shows that one half of the SL is expanded while the other half has preserved the average lattice constant. This qualitatively explains the experimentally observed disappearance of the original SL peak and the appearance of a shifted peak (Fig. 2). There is no continuous shift of the UXRD curve because there is no region in the SL which has an intermediate strain. The initially larger width of the appearing peak is readily explained by the fact that only a small spatial fraction of the SL contributes at these times

($t < 20$ ps). The very same low-frequency acoustic modes give rise to the sidebands of the substrate peak shown in Fig. 3. In particular, at $t = 39$ ps only the right shoulder exists as the substrate is compressed [blue in Fig. 5(b)] and at 73 ps also the expansion wave has entirely entered the substrate [green in Fig. 5(b)] inducing the shoulder on the left.

The atomic motion calculated from the linear-chain model also allows to extract information on the energy transport by coherent phonons. We compute the kinetic energy of the atoms from their velocity dx_i/dt and the potential energy from the stress as a function of time for both individual types of SL layer and the substrate. Figure 7 shows the total energy stored in coherent phonons in a box with a cross section of 1 cm^2.[2] At $t = 0$ all energy is quasi-instantaneously stored as potential energy in the SRO layers. As one would expect for a single excited oscillator (phonon mode), the energy is converted into kinetic energy and back to potential energy, with two maxima for each type of energy per period. The oscillation period of 3.2 ps is verified by the experimental data [1–4]. On the timescale of sound propagation ($T = D/v_{SL}$) the vibrational energy leaks into kinetic and potential energy of the substrate. Accordingly, the sum of potential and kinetic energy of the SL decays to half its initial value within 35 ps. The modulation amplitude of the potential energy is reduced by a factor of two faster, namely within 18 ps. This modulation is a direct measure of the energy stored in modes in the vicinity of the superlattice mode ω_{SL}. However, the damping of the signal oscillation amplitude observed in UXRD experiments [1, 4] is underestimated, indicating that additional factors such as anharmonic interaction and dephasing play a role. From the lattice positions $x_i(t)$ we can also calculate the average expansion of the entire SL which reaches a maximum after $T = P \cdot d_{SL}/v_{SL} = 35$ ps, in excellent agreement with previous measurements [4]. The maximum wave vector transfer q_{max} observed in Fig. 2 is used to calibrate the maximum average strain in the simulation [(1)].

After $t = 35$ ps already half of the total energy stored in longitudinal acoustic waves has moved from the SL into the contact layer and further into the substrate. It is important to note that this timescale for energy loss is not a coupling time constant, but a timescale describing the interference of the various excited normal modes, which give rise to a propagating sound wave with a particular wave vector. Unless strong differences in the acoustic impedance of the SL and the substrate lead to substantial reflection of waves at the interface, the expansion wave starting from the surface of the SL reaches the substrate after 35 ps.

---

[2]Here we plot the fraction of total energy in a fixed volume stored in the SL, the contact layer and the substrate. Plotting energy densities would not allow to see the energy conservation for the sum of energies.
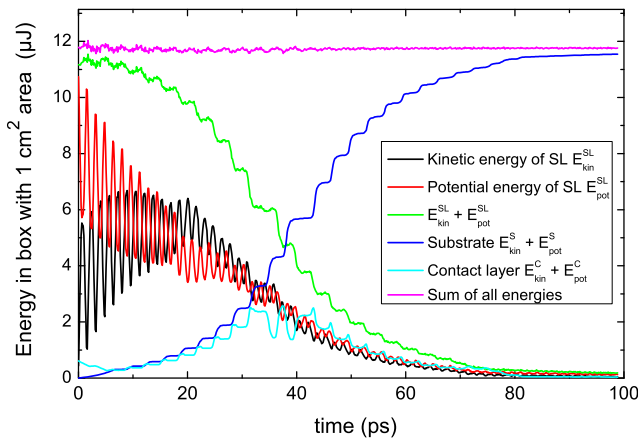
Fig. 7 Energy balance for the finite SL calculated from the linear-chain model. Both the kinetic and potential energy (stress) of the SL have two maxima per period. The energy of the propagating sound wave leaks out of the SL and travels through the contact layer (*light blue*) into the substrate (*dark blue*). We assume no considerable heat conduction on this timescale. For an infinite SL the kinetic energy would return to zero after each period (not shown), while in the present case the propagating sound wave always carries kinetic energy

In the discussion of UXRD experiments the diffraction of X-ray photons is described as resulting from the scattering by a reciprocal lattice vector and/or a phonon wavevector which describes a delocalized vibration mode. However, the X-ray-diffraction condition probes only particular spatial parts of the sample in which the Bragg condition is fulfilled, even though the vibrational mode is delocalized over the entire crystal.

The loss of modulation amplitude in UXRD signals [1–4] can be explained in our model as resulting from the coupling of the observed part of the sample (SL) to unobserved regions of the sample (substrate). The intensity modulations in the UXRD signal originate from eigenmodes with frequency ω_{SL}. Similarly, the low-frequency acoustic part of the spectrum consists of normal modes which have amplitude in the SL and the substrate. Figure 2 shows the rapid disappearance of a SL reflection and the appearance of a shifted peak which is completed after 70 ps. The dynamically interfering normal modes subsequently show no time dependence of the SL reflection which only probes the spatial region of the SL. Instead, the observation of the shoulders of the substrate peak in Fig. 3 demonstrates that at this time the coherent sound wave is in the substrate.

This implies that when calculating the coherent wave energy from the transient position of the appearing rocking curve we have to use the value for $t > 70$ ps, as this corresponds to the final state with a tensile and compressive sound wave traveling deeper into the substrate and a quasi-stationary expansion of the SL which is represented in our model by the red spacer sticks (heat expansion) in Fig. 4(c). The springs of the SL in this figure are at their equilibrium position, i.e., there is no coherent sound left in the SL. In

other words, the coherent wave energy is imposed on the sample by the initial condition which requires the compression of springs in the metallic layers of the SL (Fig. 4(b)) with respect to the final conditions at $t \to \infty$ (Fig. 4(c)). Hence, the expansive strain ϵ_{heat} for $t > 70$ ps, which is approx. 77% of the maximum expansion ϵ_{max}, measures the heat expansion of the SL and consequently the entire coherent sound energy which is encoded in the compressed springs of Fig. 4(b) at $t = 0$. For intermediate times the SL peak position is measuring a complex combination of heat expansion and additional expansion and compression due to the coherent sound waves.

Previous experiments have shown pronounced oscillations of the X-ray diffraction efficiency of SL peaks since the structure factor of the SL unit cell is modulated with the frequency ω_{SL} of the SL phonon [1–4, 7, 8]. From the linear-chain model we can deduce the energy contained in the excited modes in the vicinity of ω_{SL} (cf. Fig. 6(a)). These modes contribute approx. 30% to the total coherent mode energy because the energy per mode scales as $|A_j|^2 \omega_j^2$. The SL phonon modes itself, however, are neither responsible for the splitting of the appearing peak nor for the shoulders of the substrate. Instead, within the SL they cause the modulation of the peak intensity of SL peaks and within the substrate they give rise to sidebands to the substrate peak at $G_{STO} \pm n \cdot Q_{SL}$.

We stress that within our model, at $t = 0$ the delocalized eigenmodes are excited with their respective amplitudes A_j and merely the evolution of the relative phases of the modes leads to the complex pattern of standing and propagating sound waves in the SL and the substrate.

3.3 Quantitative calculation of rocking curves

In order to quantify the comparison of the model calculations and the measurement, the strain profile derived from the linear-chain model is used to calculate the XRD signal according to the Darwin formalism, taking into account the deformation of each unit cell [24]. The X-ray rocking curves $R(q, t)$ resulting from the strain pattern depicted in Fig. 5 are plotted in Fig. 2(a). For comparison with experiments (Fig. 2(c)) we plot the calculated difference spectra $R(q, t) - R_0(q)$ in Fig. 2(b).

For large time delay (orange curves in Fig. 2) the entire SL peak has changed its position, i.e. the difference signal is maximally negative around the initial position $q(t \leq 0)$ and reaches its positive maximum around the new position q_{max}. For intermediate times, a doublet shows up, indicating that half of the SL has already expanded whereas the remaining part still exhibits an unchanged SL period. Note that the difference of the central positions of the two peaks is larger at early times (green, blue and cyan). This corresponds to the fact that the early expansion of the layers near the surface is larger compared to the later-expanding near-substrate

layers which is due to the inhomogeneous excitation profile $\Delta(z)$. This particular feature is also visualized by the dark red color code for large expansion in the strain contour plot (Fig. 5).

While the essential features of the SL peak would be represented by a kinematic XRD theory as well, the calculation of the substrate peak (Fig. 3) and its shoulders definitely requires the used dynamical diffraction calculations. In particular, we have to add a virtually infinite STO substrate underneath the unit cells of the SL and the substrate used for the coherent phonon simulation, since the extinction length for X-rays is 1 μm at the Bragg peak and elsewhere limited by the absorption length of 10 μm. Figure 3 again shows very good agreement of simulation and experiment. Not only the effect size and timing is well reproduced, but also details like the smoothly decaying right shoulder as opposed to the decreasing in two steps seen for the left shoulder.

4 Conclusion

A simple linear-chain model is used to calculate the ultrafast motion of atoms in a superlattice coupled to a substrate upon optical excitation of the opaque layers, which results in the generation of coherent acoustic phonon modes. The surface of the SL and the SL-substrate interface break the translational symmetry of the multilayer, leading to normal modes having approximately the spatial periodicity of the SL mode, d_{SL}, and nearly equal amplitude in both the SL and the substrate. The observed energy loss from the superlattice oscillation, which has been measured previously in UXRD experiments [1–4], is predicted in this model. The time-evolution of these modes and their interference subsequently develops propagating waves which transport a large fraction of 99% of the initial energy in the coherent acoustic modes discussed in this article into the substrate within 100 ps. This requires and therefore evidences the excellent acoustic impedance matching between the epitaxial SRO and STO layers considered here. The mixed behavior originates from the fact that two small sound wavepackets are launched at each interface within the SL, giving rise to acoustic pulse trains traveling toward the surface and the substrate, respectively. The former are reflected at the sample surface and eventually also leave the SL into the substrate.

In the example discussed in this article, we demonstrate that the SL reflection does not probe the occupation of phonon modes but rather the spatial strain pattern resulting from the interference of phonon modes in the region of the SL. The loss of modulation amplitude in UXRD signals from the SL is due to the destructive interference of modes in the spatial region of the SL. The coherent sound energy initially deposited in the SL is not dissipated but coherently transported into the STO substrate by the concomitant constructive mode interference therein which forms a propagating strain wave. This strain wave is probed by UXRD in the vicinity of the substrate reflection (Fig. 3).

As presented, our model which solely describes sound propagation is able to correctly predict the observation of a peak splitting in UXRD data. In a previous publication [25] the curve splitting instead of a shifting was interpreted as a feature indicative of a phase transition. The cited publication reports additional evidence (threshold behavior, an "isosbestic point"...) for the phase transition. In the present paper we show that a peak splitting in a transient rocking curve is not sufficient to conclude a phase transition. To the best of our knowledge this is the first report on the splitting of a Bragg peak of a thin film or SL due to sound propagation. As most thin film samples are grown on substrates, we expect the discussed features to appear in several future UXRD studies.

Appendix

We divide (2) by m_i and define $\Delta_i(t) = F_i(t)/m_i$, $\kappa_{i,i} = -(k_i + k_{i+1})/m_i$ and $\kappa_{i,i+1} = \kappa_{i+1,i} = k_{i+1}/m_i$. Moreover, $\kappa_{i,j} = 0$ if $|i - j| > 1$, since only nearest neighbors are connected by springs. The values for $i = 1$ and $i = N$ must be set according to the correct boundary conditions, namely, $\kappa_{1,1} = -(k_2)/m_1$ and $\kappa_{N,N} = -(k_N)/m_N$. For the surface of the SL ($i = 1$) this yields a proper description for all times. The layer $i = N$ is chosen so deep in the substrate that it does not move within the simulated timescale. This gives the system of equations

$$\ddot{x}_i + \sum_{n=1}^{N} \kappa_{i,n} x_n = \Delta_i(t). \tag{4}$$

The homogeneous system ($\Delta = 0$) can be recast into the vector equation

$$\frac{d^2}{dt^2}\mathbf{X} = \mathbf{K}\mathbf{X} \tag{5}$$

where $\mathbf{X} = (x_1, \ldots, x_N)^T$ is the vector containing all displacements and $\mathbf{K}$ is the tri-diagonal matrix

$$\mathbf{K} = \begin{pmatrix} \kappa_{1,1} & \kappa_{1,2} & & & & & \\ \kappa_{2,1} & \ddots & \ddots & & & & \\ & \ddots & \kappa_{i,i} & \kappa_{i,i+1} & & & \\ & & \kappa_{i+1,i} & \ddots & \ddots & & \\ & & & \ddots & \kappa_{N-1,N-1} & \kappa_{N-1,N} \\ & & & & \kappa_{N,N-1} & \kappa_{N,N} \end{pmatrix} \tag{6}$$

where we omitted the zero-entries for clarity. As mentioned above, $\kappa_{i,i+1} = \kappa_{i+1,i}$, which ensures that $\mathbf{K}$ is real and symmetric and thus all its eigenvalues are real.

The general solution of (5) is given by (3). The set of eigenmodes is represented by the eigenvectors

$$\Xi_j = \begin{pmatrix} \xi_1^j \\ \vdots \\ \xi_N^j \end{pmatrix} \tag{7}$$

which correspond to the eigenvalues (eigenfrequencies) ω_j of the system, respectively, and which are found by diagonalization of $\mathbf{K}$. Since for $t \geq 0$ we assume $\Delta(z,t) = \Delta(z)$ to be time independent, we can rewrite the inhomogeneous vector equation as

$$\frac{d^2}{dt^2}\mathbf{X} - \mathbf{K}\mathbf{X} = \Delta \tag{8}$$

$$\Leftrightarrow \frac{d^2}{dt^2}\left(\mathbf{X} + \mathbf{K}^{-1}\Delta\right) - \mathbf{K}\left(\mathbf{X} + \mathbf{K}^{-1}\Delta\right) = 0 \tag{9}$$

$$\Leftrightarrow \frac{d^2}{dt^2}(\mathbf{X}^{\infty}) - \mathbf{K}(\mathbf{X}^{\infty}) = 0 \tag{10}$$

We define the atomic positions z_i^{∞} for $t \to \infty$ as the new equilibrium positions for the new coordinates $\mathbf{X}^{\infty} = \mathbf{X} - \mathbf{K}^{-1}\Delta$, such that $z_i(t) = z_i^0 + x_i(t) = z_i^{\infty} + x_i^{\infty}(t)$. The particular solution of the homogeneous equation for the new coordinates, i.e. the complex coefficients A_j, are found by reading the initial conditions for $t = 0$ from Fig. 4(b) and (c) and recalling that in $x_i^{\infty}(t) = z_i^0 - z_i^{\infty} + x_i(t)$ the relation $x_i(t) = 0$ holds. Hence, we find

$$x_i^{\infty}(0) = z_i^0 - z_i^{\infty} = \sum_{j=i+1}^{N} l_j \quad \text{and} \quad \frac{d}{dt}x_i^{\infty}(0) = 0 \tag{11}$$

for $i = 1, \ldots, N$, where l_j is the length of the jth stick depicting the photoinduced stress which thereby determines the complex coefficients A_j in (3).

References

1. M. Herzog, W. Leitenberger, R. Shayduk, R.M. van der Veen, C.J. Milne, S.L. Johnson, I. Vrejoiu, M. Alexe, D. Hesse, M. Bargheer, Ultrafast manipulation of hard X-rays by efficient Bragg switches. Appl. Phys. Lett. **96**, 161906 (2010)
2. M. Woerner, C. v. Korff Schmising, M. Bargheer, N. Zhavoronkov, I. Vrejoiu, D. Hesse, M. Alexe, T. Elsaesser, Ultrafast structural dynamics of perovskite superlattices. Appl. Phys. A **96**, 83 (2009)
3. C. v. Korff Schmising, A. Harpoeth, N. Zhavoronkov, Z. Ansari, C. Aku-Leh, M. Woerner, T. Elsaesser, M. Bargheer, M. Schmidbauer, I. Vrejoiu, D. Hesse, M. Alexe, Ultrafast magnetostriction and phonon-mediated stress in a photoexcited ferromagnet. Phys. Rev. B **78**, 060404(R) (2008)
4. C. v. Korff Schmising, M. Bargheer, M. Kiel, N. Zhavoronkov, M. Woerner, T. Elsaesser, I. Vrejoiu, D. Hesse, M. Alexe, Accurate time delay determination for femtosecond X-ray diffraction experiments. Appl. Phys. B **88**, 1 (2007)
5. M. Cardona, *Light Scattering in Solids V Superlattices and Other Microstructures*, 2nd edn. Topics in Applied Physics (Springer, Berlin, 1989)
6. C. Colvard, T.A. Gant, M.V. Klein, R. Merlin, R. Fischer, H. Morkoc, A.C. Gossard, Folded acoustic and quantized optic phonons in (gaal)as superlattices. Phys. Rev. B **31**(4), 2080 (1985)
7. M. Bargheer, N. Zhavoronkov, Y. Gritsai, J.C. Woo, D.S. Kim, M. Woerner, T. Elsaesser, Science **306**, 1771 (2004)
8. C. v. Korff Schmising, M. Bargheer, M. Kiel, N. Zhavoronkov, M. Woerner, T. Elsaesser, I. Vrejoiu, D. Hesse, M. Alexe, Coupled ultrafast lattice and polarization dynamics in ferroelectric nanolayers. Phys. Rev. Lett. **98**(25), 257601 (2007)
9. S. Yamanaka, T. Maekawa, H. Muta, T. Matsuda, S. Kobayashi, K. Kurosaki, Thermophysical properties of SrHfO₃ and SrRuO₃. J. Solid State Chem. **177**, 3484 (2004)
10. Y.H. Ren, M. Trigo, R. Merlin, V. Adyam, Q. Li, Generation and detection of coherent longitudinal acoustic phonons in the La₀.₆₇Sr₀.₃₃MnO₃ thin films by femtosecond light pulses. Appl. Phys. Lett. **90**, 251918 (2007)
11. Bauer, *Multilayers*, 2nd edn. (Springer, Berlin, 1998)
12. C. Rose-Petruck, R. Jimenez, T. Guo, A. Cavalleri, C.W. Siders, F. Rksi, J.A. Squier, B.C. Walker, K.R. Wilson, C.P.J. Barty, Picosecond-milliangstrom lattice dynamics measured by ultrafast X-ray diffraction. Nature **398**(6725), 310–312 (1999)
13. A.M. Lindenberg, I. Kang, S.L. Johnson, T. Missalla, P.A. Heimann, Z. Chang, J. Larsson, P.H. Bucksbaum, H.C. Kapteyn, H.A. Padmore, R.W. Lee, J.S. Wark, R.W. Falcone, Time-resolved X-ray diffraction from coherent phonons during a laser-induced phase transition. Phys. Rev. Lett. **84**(1), 111–114 (2000)
14. D.A. Reis, M.F. DeCamp, P.H. Bucksbaum, R. Clarke, E. Dufresne, M. Hertlein, R. Merlin, R. Falcone, H. Kapteyn, M.M. Murnane, J. Larsson, T. Missalla, J.S. Wark, Probing impulsive strain propagation with X-ray pulses. Phys. Rev. Lett. **86**(14), 3072–3075 (2001)
15. K. Sokolowski-Tinten, C. Blome, C. Dietrich, A. Tarasevitch, M. Horn von Hoegen, D. von der Linde, A. Cavalleri, J. Squier, M. Kammler, Femtosecond X-ray measurement of ultrafast melting and large acoustic transients. Phys. Rev. Lett. **87**(22), 225701 (2001)
16. M. Trigo, Y.M. Sheu, D.A. Arms, J. Chen, S. Ghimire, R.S. Goldman, E. Landahl, R. Merlin, E. Peterson, M. Reason, D.A. Reis, Probing unfolded acoustic phonons with X-rays. Phys. Rev. Lett. **101**(2), 025505 (2008)
17. A. Cavalleri, C.W. Siders, F.L.H. Brown, D.M. Leitner, C. Tóth, J.A. Squier, C.P.J. Barty, K.R. Wilson, K. Sokolowski-Tinten, M. Horn von Hoegen, D. von der Linde, M. Kammler, Anharmonic lattice dynamics in germanium measured with ultrafast X-ray diffraction. Phys. Rev. Lett. **85**(3), 586–589 (2000)
18. J. Larsson, A. Allen, P.H. Bucksbaum, R.W. Falcone, A. Lindenberg, G. Naylor, T. Missalla, D.A. Reis, K. Scheidt, A. Sjögren, P. Sondhauss, M. Wulff, J.S. Wark, Picosecond X-ray diffraction studies of laser-excited acoustic phonons in insb. Appl. Phys. A **75**, 467–478 (2002)

19. F. Zamponi, Z. Ansari, C. v. Korff Schmising, P. Rothhardt, N. Zhavoronkov, M. Woerner, T. Elsaesser, M. Bargheer, T. Trobitzsch-Ryll, M. Haschke, Femtosecond hard X-ray plasma sources with a kilohertz repetition rate. Appl. Phys. A **96**, 51 (2009)

20. P. Beaud, S.L. Johnson, A. Streun, R. Abela, D. Abramsohn, D. Grolimund, F. Krasniqi, T. Schmidt, V. Schlott, G. Ingold, Spatiotemporal stability of a femtosecond hard–X-ray undulator source studied by control of coherent optical phonons. Phys. Rev. Lett. **99**(17), 174801 (2007)

21. J. Li, R. Clinite, X. Wang, J. Cao, Simulation of ultrafast heating induced structural dynamics using a one-dimensional spring model. Phys. Rev. B **80**(1), 014304 (2009)

22. P. Kostic, Y. Okada, N.C. Collins, Z. Schlesinger, J.W. Reiner, L. Klein, A. Kapitulnik, T.H. Geballe, M.R. Beasley, Non-Fermi-liquid behavior of srruo3: Evidence from infrared conductivity. Phys. Rev. Lett. **81**(12), 2498 (1998)

23. M. Bargheer, N. Zhavoronkov, J.C. Woo, D.S. Kim, M. Woerner, T. Elsaesser, Excitation mechanisms of coherent phonons unravelled by femtosecond X-ray diffraction. Phys. Status Solidi (b) **243**(10), 2389 (2006)

24. S.A. Stepanov, E.A. Kondrashkina, R. Köhler, D.V. Novikov, G. Materlik, S.M. Durbin, Dynamical X-ray diffraction of multilayers and superlattices: Recursion matrix extension to grazing angles. Phys. Rev. B **57**(8), 4829–4841 (1998)

25. N. Gedik, Y. Ding-Shyue, G. Logvenov, I. Bozovic, A.H. Zewail, Nonequilibrium phase transitions in cuprates observed by ultrafast electron crystallography. Science **316**(5823), 425 (2007)